(Preprint) AAS 23-291

IMPACT OF DIFFERENT COORDINATE SETS ON THE PERFORMANCE OF CONVEX LOW-THRUST TRAJECTORY OPTIMIZATION

Christian Hofmann [*], Andrea C. Morelli [†], and Francesco Topputo[‡]

The choice of the coordinate representation of the state vector has a considerable impact on the performance of low-thrust trajectory optimization methods. This is especially true for sequential convex programming techniques due to the successive linearization of nonlinear dynamics. In this work, various coordinate representations are assessed for the low-thrust trajectory optimization problem. In particular, standard coordinate sets are considered (i.e. Cartesian, spherical, and modified equinoctial elements), and non-standard coordinates (two sets based on Kustaanheimo-Stiefel and modified orbital elements) are introduced that result in linear dynamics in the unperturbed case. In addition, two nonlinearity indices tailored to convex optimization are proposed to assess the nonlinearity of the dynamical system.

INTRODUCTION

The equations of motion form a fundamental part in astrodynamics. Before solving an optimal control problem, the equations that govern the motion of the spacecraft (or any other object) are to be derived. Cartesian coordinates are probably the most common and popular representation of the dynamics. Yet, several different sets of coordinates have been developed in the past decades. The reason is that the choice of the coordinates can have a considerable impact on the performance of numerical methods to solve problems related to astrodynamics.[1] Spherical coordinates (or polar coordinates in the planar case) seem to be a natural choice to describe the translational motion of a spacecraft around a body. Several works use these coordinates to solve the low-thrust trajectory optimization problem.[2–4] Cylindrical coordinates are often used in shape-based methods where the trajectory is approximated with certain functions.[5] Canonical elements such as Delaunay[6] and Poincaré[7] elements are advantageous for perturbation problems due to the simplifications that can be made when the perturbing acceleration is considered small. Equinoctial elements were developed to overcome the singularities of classical orbital elements.[8] They are a popular choice for many-revolution transfers in indirect methods because five out of six elements are constant for the unperturbed motion.[9–11] Alternative representations such as quaternion-like elements for the initial value problem[12] or coordinates that use the angular momentum and eccentricity vectors[13] for high-inclination orbital transfers were developed only recently.

[*]Ph.D. Candidate, Department of Aerospace Science and Technology, Via La Masa 34, 20156 Milan, Italy. Email: christian.hofmann@polimi.it.

[†]Ph.D. Candidate, Department of Aerospace Science and Technology, Via La Masa 34, 20156 Milan, Italy. Email: andreacarlo.morelli@polimi.it.

[‡]Professor, Department of Aerospace Science and Technology, Via La Masa 34, 20156 Milan, Italy. Email: francesco.topputo@polimi.it.

The choice of the coordinates becomes even more crucial for nonlinear optimization methods where linearization is involved. An example is sequential convex programming (SCP), where the nonlinear dynamics are successively linearized to obtain an approximate solution of the nonlinear optimal control problem. Even though many constraints can be relaxed and convexified, dynamics are usually approximated using a first-order Taylor series. Understanding the impact of the coordinate set on the performance of SCP is therefore of utmost practical interest. Yet, previous research activities lack a thorough assessment and comparison of relevant state vector choices for convex low-thrust trajectory optimization. In other works,[1] an indirect method is used to investigate the performance of several minimal coordinate sets for the low-thrust fuel-optimal trajectory optimization problem, but the results cannot be applied directly to the SCP approach due to the fundamentally different characteristics of both methods.

Besides an explicit comparison of the performance of different representations of the dynamics, a nonlinearity index was introduced in previous work[14] to compare the nonlinearity of dynamical systems. This metric is intended to measure how nonlinear a dynamical system is for unperturbed initial value problems. This approach was later extended to include control terms.[15] More recently, an augmented nonlinearity index was introduced to account for state-costate dynamics in indirect methods.[16] This was applied to the spacecraft attitude control problem.

The contribution of this work is threefold. First, we introduce a set of modified orbital elements (MOE) and two variants of the Kustaanheimo-Stiefel (KS) coordinates for convex low-thrust trajectory optimization. These sets express the unperturbed two-body dynamics in linear (or weakly nonlinear) form, which is advantageous when solving optimal control problems via SCP as the nonlinear dynamics are usually linearized. Secondly, we introduce two nonlinearity indices to assess the level of nonlinearity of the proposed coordinate sets. Finally, we perform a thorough assessment of the convergence and performance properties of the classical (Cartesian, spherical, cylindrical, modified equinoctial elements) and the non-standard coordinate sets when poor initial guesses are provided.

The paper is structured as follows. Section II describes the convexified optimal control problem and the discretization method. The nonlinearity indices are introduced in Section III, and Section IV addresses the coordinate sets. The results are presented in Section V, and Section VI concludes this paper.

PROBLEM STATEMENT

We consider the problem of finding the interplanetary minimum-fuel trajectory of a spacecraft subject to the gravitational attraction of the Sun and the thrust provided by a low-thrust engine. Such a problem has nonlinear and nonconvex dynamics regardless of the set of coordinates. We write the dynamics in the form

$$\mathbf{f}(\mathbf{x}, \mathbf{u}) = \mathbf{g}(\mathbf{x}) + \mathbf{B}(\mathbf{x})\,\mathbf{u} \tag{1}$$

where $\mathbf{g}(\mathbf{x})$ and $\mathbf{B}(\mathbf{x})$ are generic functions of the state variables $\mathbf{x}$, and $\mathbf{u}$ are the controls. The convex form of the low-thrust trajectory optimization then reads[17]

$$\underset{\mathbf{u}(t)}{\text{minimize}} \quad -w(t_f) + \lambda \left\|\boldsymbol{\nu}(t)\right\|_1 + \lambda \max(0, \psi(t)) \tag{2a}$$

$$\text{subject to:} \quad \dot{\mathbf{x}}(t) = \bar{\mathbf{f}} + \nabla_x \bar{\mathbf{f}}\ (\mathbf{x}(t) - \bar{\mathbf{x}}(t)) + \nabla_u \bar{\mathbf{f}}\ (\mathbf{u}(t) - \bar{\mathbf{u}}(t)) + \boldsymbol{\nu}(t) \tag{2b}$$

$$\Gamma(t) \leq T_{\max}\, \mathrm{e}^{-\bar{w}(t)}\, [1 - w(t) + \bar{w}(t)] + \psi(t) \tag{2c}$$

$$\|\boldsymbol{\tau}(t)\|_2 \leq \Gamma(t) \tag{2d}$$
$$\|\mathbf{x}(t) - \bar{\mathbf{x}}(t)\|_1 \leq R \tag{2e}$$
$$\mathbf{x}_{\text{pv}}(t_0) = \mathbf{x}_0,\ w(t_0) = w_0 \tag{2f}$$
$$\mathbf{x}_{\text{pv}}(t_f) = \mathbf{x}_f \tag{2g}$$
$$\mathbf{x}_l \leq \mathbf{x}(t) \leq \mathbf{x}_u,\ \mathbf{u}_l \leq \mathbf{u}(t) \leq \mathbf{u}_u \tag{2h}$$

where the bar denotes the reference value of the quantity, and

$$\bar{\mathbf{f}} \coloneqq \mathbf{f}\left(\bar{\mathbf{x}}(t), \bar{\mathbf{u}}(t)\right) \tag{3}$$

The objective function of the problem is given by Eq. (2a), where $w(t_f)$ is the modified spacecraft mass at the final time t_f, λ a penalty factor, and $\boldsymbol{\nu}$ and ψ are slack variables to avoid artificial infeasibility. Equation (2b) describes the linearized dynamics, Eqs. (2c) and (2d) the control constraints. The trust-region constraint in Eq. (2e) with radius R is imposed to keep the linearization close to the reference. Equations (2f) and (2g) express the initial and final boundary conditions, and the subscript $(\cdot)_{\text{pv}}$ refers to the states that describe the position and the velocity of the spacecraft. Equation (2h) represents the upper (subscript u) and lower bounds (subscript l) on the state and control variables, respectively. The control variables $\mathbf{u} \in \mathbb{R}^4$ are defined as $\mathbf{u} \coloneqq [\boldsymbol{\tau}^\top, \Gamma]^\top$ where $\boldsymbol{\tau} \in \mathbb{R}^3$ and $\Gamma \in \mathbb{R}$.

The convexified optimal control problem is discretized using the first-order-hold method (FOH) where the dynamical constraints take the following form:[17]

$$\mathbf{x}_{k+1} = \mathbf{A}_k\, \mathbf{x}_k + \mathbf{B}_k^-\, \mathbf{u}_k + \mathbf{B}_k^+\, \mathbf{u}_{k+1} + \mathbf{q}_k + \boldsymbol{\nu}_k \tag{4}$$

with certain matrices $\mathbf{A}_k$, $\mathbf{B}_k^-$, $\mathbf{B}_k^+$, and the vector $\mathbf{q}_k$, $k = 1, \ldots, n-1$ being the kth discretization point. The obtained convex optimization problem is solved using a trust-region based SCP algorithm.[18]

NONLINEARITY INDEX

We are interested in assessing different state vector representations for the low-thrust trajectory optimization problem using SCP where the nonlinear dynamics are successively linearized about a reference. We therefore expect to benefit from coordinates where this first-order Taylor approximation is as accurate as possible. We propose the nonlinearity index Ξ^f that evaluates the original nonlinear dynamics function $\mathbf{f}_k^{\text{nonlin}}$ and its first-order Taylor series $\mathbf{f}_k^{\text{lin}}$ at each node $k = 1, \ldots, n$:

$$\Xi_k^f \coloneqq \frac{\|\mathbf{f}_k^{\text{nonlin}} - \mathbf{f}_k^{\text{lin}}\|}{\|\mathbf{f}_k^{\text{nonlin}}\|}, \quad k = 1, \ldots, n \tag{5}$$

where

$$\mathbf{f}^{\text{lin}} = \mathbf{f}\left(\bar{\mathbf{x}}, \bar{\mathbf{u}}\right) + \nabla_x \mathbf{f}\left(\bar{\mathbf{x}}, \bar{\mathbf{u}}\right)\ (\mathbf{x} - \bar{\mathbf{x}}) + \nabla_u \mathbf{f}\left(\bar{\mathbf{x}}, \bar{\mathbf{u}}\right)\ (\mathbf{u} - \bar{\mathbf{u}}) \tag{6}$$

The division by the norm is added as a normalization to account for the different domains of the variables in each set. Equation (5) essentially compares the function values of the nonlinear functions with the values of the first-order Taylor series evaluated at a reference point $(\bar{\mathbf{x}}, \bar{\mathbf{u}})$. Our rationale is that the linearization error $E(x)$ becomes zero when $\Delta x \to 0$:

$$\lim_{\Delta x \to 0} E(x) = \lim_{\Delta x \to 0} f(\bar{x} + \Delta x) - \left[f(\bar{x}) + f'(\bar{x})\, \Delta x\right] = 0 \tag{7}$$

Therefore, the index indicates how well the linearization is able to represent the original nonlinear function. Smaller values suggest better approximations, and a value of zero means that the linearization is exact.

As the index depends on the deviation from a reference point, we select a sufficiently large number N of perturbed trajectories that lie in the neighborhood of the reference. The nonlinearity index Ξ_k^f at each node is then given by the average over N samples:

$$\Xi_k^f := \frac{1}{N} \sum_{i=1}^{N} \Xi_{k,i}^f, \quad k = 1, \ldots, n, \; i = 1, \ldots, N \tag{8}$$

Remark: It is also possible to use the maximum instead of the mean value for computing the index. Our simulations suggest that there is no significant difference.

In FOH, the state transition matrix is used to discretize the problem. The dynamics are integrated, and the state at t_{k+1} is obtained by evaluating Eq. (4). The violations of the nonlinear dynamical constraints c_k^{nonlin} are computed by comparing the states at the end of a segment k:

$$c_k^{\text{nonlin}} = \left\| \mathbf{x}_{k+1} - \mathbf{x}_{k+1}^{\text{nonlin}} \right\|, \quad k = 1, \ldots, n-1 \tag{9}$$

where $\mathbf{x}_{k+1}$ denotes the state at t_{k+1} obtained from the optimization, and $\mathbf{x}_{k+1}^{\text{nonlin}}$ is computed using the nonlinear dynamics:

$$\mathbf{x}_{k+1}^{\text{nonlin}} = \mathbf{x}_k + \int_{t_k}^{t_{k+1}} \mathbf{f}_{\text{nonlin}}(\mathbf{x}(\zeta), \mathbf{u}(\zeta)) \, \mathrm{d}\zeta, \quad k = 1, \ldots, n-1 \tag{10}$$

where $\mathbf{x}_k \equiv \mathbf{x}(t_k)$ is also the optimized state. As $\mathbf{x}_{k+1}$ is obtained using Eq. (4), the state transition matrix is required, and hence, the integration of the Jacobian matrices. Therefore, even if two coordinate sets yield a similar nonlinearity index Ξ^f, the constraint violation can be large as the error accumulates during the integration. We thus propose a second nonlinearity index Ξ^x that is defined as follows:

$$\Xi_k^x := \frac{\|\mathbf{x}_{k+1}^{\text{nonlin}} - \mathbf{x}_{k+1}^{\text{lin}}\|}{\|\mathbf{x}_{k+1}^{\text{nonlin}}\|}, \quad k = 1, \ldots, n-1 \tag{11}$$

It evaluates the difference of the integrated states obtained using the nonlinear dynamics and the state transition matrix, respectively.

Generation of Perturbed Trajectories

Given a reference trajectory $\bar{\mathbf{x}}(t)$ and its corresponding initial condition $\bar{\mathbf{x}}(t_0)$, we define a set of N worst-case initial condition variations $\delta\mathbf{x}_i(t_0)$, $i = 1, \ldots, N$ with $\|\delta\mathbf{x}_i(t_0)\| = \delta x_{\max}$, similar to what has been defined in previous work.[14] In particular, we use Cartesian coordinates to define

$$\delta x_{\max} = \left\| \begin{bmatrix} \delta\mathbf{r}_{\max} \\ \delta\mathbf{v}_{\max} \end{bmatrix} \right\| \tag{12}$$

where $\delta\mathbf{r}_{\max} \in \mathbb{R}^3$ and $\delta\mathbf{v}_{\max} \in \mathbb{R}^3$ are arbitrary entries that define the position and velocity variations, respectively. The worst-case initial conditions therefore lie on a N-dimensional sphere of radius $\delta x_{\max}$. The perturbed initial condition $\mathbf{x}_i(t_0)$ is then

$$\mathbf{x}_i(t_0) = \bar{\mathbf{x}}(t_0) + \delta\mathbf{x}_i(t_0), \quad i = 1, \ldots, N \tag{13}$$

Similarly, worst-case control variations $\delta\mathbf{u}_i(t_k)$ with $\|\delta\mathbf{u}_i(t_k)\| = \|\delta\mathbf{u}_{\max}\| = \delta u_{\max}$ are defined at each time instant t_k, $k = 1, \ldots, n$, $i = 1, \ldots, N$, The perturbed control profiles $\mathbf{u}_i(t_k)$ read

$$\mathbf{u}_i(t_k) = \bar{\mathbf{u}}(t_k) + \delta\mathbf{u}_i(t_k), \quad i = 1, \ldots, N,\ i = 1, \ldots, n \tag{14}$$

In our case, $\delta\mathbf{u}_i(t_k) \equiv \delta\boldsymbol{\tau}_i(t_k)$, i.e. we only perturb the components $\boldsymbol{\tau} \in \mathbb{R}^3$ and then compute the magnitude using $\Gamma_i(t_k) = \|\boldsymbol{\tau}_i(t_k)\|$.

The nonlinear dynamics are then integrated using the perturbed control profiles $\mathbf{u}_i(t)$ obtained from Eq. (14) and the perturbed initial conditions $\mathbf{x}_i(t_0)$. The resulting N state trajectories $\mathbf{x}_i(t)$ deviate from the reference by $\delta\mathbf{x}_i(t)$:

$$\mathbf{x}_i(t) = \bar{\mathbf{x}}(t) + \delta\mathbf{x}_i(t), \quad i = 1, \ldots, N \tag{15}$$

These trajectories are then transformed into the other coordinate sets to determine the nonlinearity indices.

COORDINATE SETS

Even though there are many different coordinate choices, previous works suggest that any set of orbital elements often performs similar or worse compared to modified equinoctial elements (MEE). Therefore, we select MEE as the only standard set of orbital elements. In addition to the most popular state representations, i.e. Cartesian, cylindrical, and spherical coordinates, we consider a recently-developed set of modified orbital elements (MOE).[19] The main difference compared with other sets in the literature is that the dynamics are linear in the unperturbed case due to a time regularization. Moreover, we also take into account the non-minimal Kustaanheimo-Stiefel (KS) coordinates.[20] The main benefit of both representations is that the dynamics are (weakly) nonlinear in the unperturbed case. This is expected to be beneficial for the successive linearization approach in SCP.

We define the unperturbed $\mathbf{g}(\mathbf{x})$ and perturbed $\mathbf{B}(\mathbf{x})$ terms in Eq. (1) to be either linear, weakly nonlinear, or nonlinear. Table 1 characterizes the proposed coordinate systems in terms of the level of nonlinearity, the number of state variables (without considering the mass), and the number of slow and fast variables, slow meaning that the element is constant when no perturbations are present. The selected coordinates cover a wide variety of combinations. The linear terms of each coordinate system are advantageous because no approximations are introduced when building the convex subproblems in Eqs. (2). However, as highlighted in Table 1, no state vector representation has only linear terms. It is therefore not straightforward to indicate a certain set of coordinates as the most suitable.

In the following subsections, the expressions for $\mathbf{g}(\mathbf{x})$ and $\mathbf{B}(\mathbf{x})$ of the different coordinate sets are presented. For the sake of conciseness, the length of the subsections for the well-known Cartesian, cylindrical, and spherical coordinates as well as MEE are kept as short as possible. The modified orbital elements and KS coordinates are explained in more detail as most readers may not be familiar with them. If not stated otherwise, the control components are defined using the unit vectors of the corresponding coordinate frame.

Table 1: Overview of the considered coordinate sets.

Coordinates	Unpert. dynamics $\mathbf{g}(\mathbf{x})$	Pert. dynamics $\mathbf{B}(\mathbf{x})$	# states	Slow / fast variables
Cartesian	Nonlinear	Constant	6	0 / 6
Cylindrical	Nonlinear	Constant	6	0 / 6
Spherical	Nonlinear	Constant	6	0 / 6
MEE	Weakly nonlinear	Nonlinear	6	5 / 1
MOE	Linear*	Nonlinear	6†	2 / 4†
KS_ξ	Weakly nonlinear*	Nonlinear	9†	1 / 8†
KS_E	Linear*	Nonlinear	9†	1 / 8†

* The dynamics become nonlinear if time is added as a state variable.
† The number increases by one if time is added as a state variable.

Cartesian

The state $\mathbf{x} \in \mathbb{R}^7$ and control $\mathbf{u} \in \mathbb{R}^4$ vectors are

$$\mathbf{x}_{\text{cart}} = \left[\mathbf{r}^\top, \mathbf{v}^\top, w\right]^\top = [x, y, z, v_x, v_y, v_z, w]^\top \tag{16}$$

$$\mathbf{u}_{\text{cart}} = \left[\boldsymbol{\tau}^\top, \Gamma\right]^\top \tag{17}$$

The quantities $\mathbf{g}_{\text{cart}}(\mathbf{x})$ and $\mathbf{B}_{\text{cart}}(\mathbf{x})$ are

$$\mathbf{g}_{\text{cart}}(\mathbf{x}) = \begin{bmatrix} v_x \\ v_y \\ v_z \\ -\frac{\mu\, x}{(x^2+y^2+z^2)^{3/2}} \\ -\frac{\mu\, y}{(x^2+y^2+z^2)^{3/2}} \\ -\frac{\mu\, z}{(x^2+y^2+z^2)^{3/2}} \\ 0 \end{bmatrix}, \quad \mathbf{B}_{\text{cart}}(\mathbf{x}) = \begin{bmatrix} & & \mathbf{0}_{3\times 4} & \\ 1 & 0 & 0 & 0 \\ 0 & 1 & 0 & 0 \\ 0 & 0 & 1 & 0 \\ 0 & 0 & 0 & -\frac{1}{g_0\, I_{\text{sp}}} \end{bmatrix} \tag{18}$$

Spherical Coordinates

The state $\mathbf{x} \in \mathbb{R}^7$ and control $\mathbf{u} \in \mathbb{R}^4$ vectors are

$$\mathbf{x}_{\text{sph}} = [r, \theta, \phi, v_r, v_\theta, v_\phi, w]^\top \tag{19}$$

$$\mathbf{u}_{\text{sph}} = \left[\boldsymbol{\tau}^\top, \Gamma\right]^\top \tag{20}$$

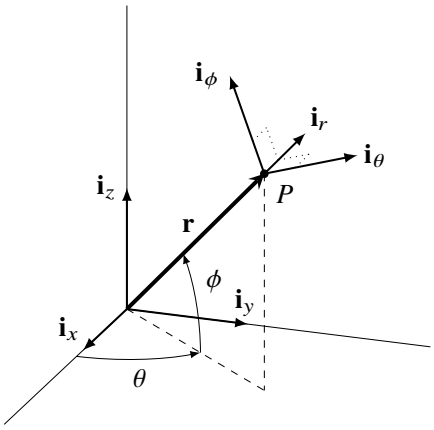

Figure 1: Spherical coordinates and rotating coordinate system.

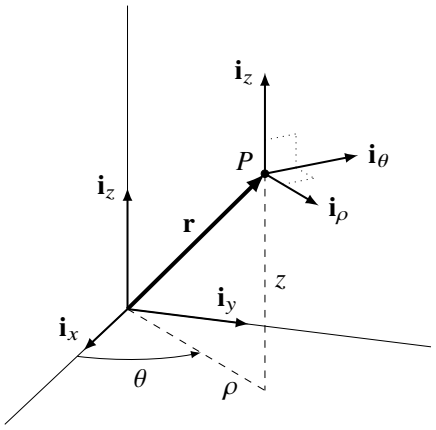

Figure 2: Cylindrical coordinates and rotating coordinate system.

where r, θ, and ϕ denote the radial distance, azimuthal, and polar angle, respectively (see Fig. 1). The quantities $\mathbf{g}_{\text{sph}}(\mathbf{x})$ and $\mathbf{B}_{\text{sph}}(\mathbf{x})$ are

$$\mathbf{g}_{\text{sph}}(\mathbf{x}) = \begin{bmatrix} v_r \\ \frac{v_\theta}{r} \\ \frac{v_\phi}{r\sin(\theta)} \\ \frac{v_\theta^2}{r} + \frac{v_\phi^2}{r} - \frac{\mu}{r^2} \\ -\frac{v_r v_\theta}{r} + \frac{v_\phi^2 \cos(\theta)}{r\sin(\theta)} \\ -\frac{v_r v_\phi}{r} - \frac{v_\theta v_\phi \cos(\theta)}{r\sin(\theta)} \\ 0 \end{bmatrix}, \quad \mathbf{B}_{\text{sph}}(\mathbf{x}) = \begin{bmatrix} \mathbf{0}_{3\times 4} \\ 1 & 0 & 0 & 0 \\ 0 & 1 & 0 & 0 \\ 0 & 0 & 1 & 0 \\ 0 & 0 & 0 & -\frac{1}{g_0 I_{\text{sp}}} \end{bmatrix} \tag{21}$$

Cylindrical Coordinates

The state $\mathbf{x} \in \mathbb{R}^7$ and control $\mathbf{u} \in \mathbb{R}^4$ vectors are

$$\mathbf{x}_{\text{cyl}} = [\rho, \theta, z, v_\rho, v_\theta, v_z, w]^\top \tag{22}$$

$$\mathbf{u}_{\text{cyl}} = \left[\boldsymbol{\tau}^\top, \Gamma\right]^\top \tag{23}$$

where ρ, θ, and z denote the radial distance from the z-axis, azimuthal angle, and the distance from the reference plane, respectively (see Fig. 2). The quantities $\mathbf{g}_{\text{cyl}}(\mathbf{x})$ and $\mathbf{B}_{\text{cyl}}(\mathbf{x})$ are

$$\mathbf{g}_{\text{cyl}}(\mathbf{x}) = \begin{bmatrix} v_\rho \\ \frac{v_\theta}{\rho} \\ v_z \\ \frac{v_\theta^2}{\rho} - \frac{\mu\,\rho}{(\rho^2+z^2)^{3/2}} \\ -\frac{v_\rho v_\theta}{\rho} \\ -\frac{\mu\, z}{(\rho^2+z^2)^{3/2}} \\ 0 \end{bmatrix}, \quad \mathbf{B}_{\text{cyl}}(\mathbf{x}) = \begin{bmatrix} \mathbf{0}_{3\times 4} \\ 1 & 0 & 0 & 0 \\ 0 & 1 & 0 & 0 \\ 0 & 0 & 1 & 0 \\ 0 & 0 & 0 & -\frac{1}{g_0 I_{\text{sp}}} \end{bmatrix} \tag{24}$$

Modified Equinoctial Elements

The state $\mathbf{x} \in \mathbb{R}^7$ and control $\mathbf{u} \in \mathbb{R}^4$ vectors are

$$\mathbf{x}_{\text{MEE}} = [p, e_x, e_y, h_x, h_y, l, w]^\top \tag{25}$$

$$\mathbf{u}_{\text{MEE}} = \left[\boldsymbol{\tau}^\top, \Gamma\right]^\top \tag{26}$$

The relationship between modified equinoctial and classical orbital elements is given by

$$p = a\left(1 - e^2\right) \tag{27}$$

$$e_x = e\,\cos\left(\omega + \Omega\right) \tag{28}$$

$$e_y = e\,\sin\left(\omega + \Omega\right) \tag{29}$$

$$h_x = \tan\left(i/2\right)\,\cos\Omega \tag{30}$$

$$h_y = \tan\left(i/2\right)\,\sin\Omega \tag{31}$$

$$l = \omega + \Omega + \vartheta \tag{32}$$

where p denotes the semilatus rectum, a the semi-major axis, e the eccentricity, ω the argument of periapsis, Ω the longitude of the ascending node, i the inclination, l the true longitude, and ϑ the true anomaly. The quantities $\mathbf{g}_{\text{MEE}}(\mathbf{x})$ and $\mathbf{B}_{\text{MEE}}(\mathbf{x})$ are[9]

$$\mathbf{g}_{\text{MEE}}(\mathbf{x}) = \left[0, 0, 0, 0, 0, \sqrt{\mu\, p}\,\left(\frac{\sigma}{p}\right)^2\right]^\top \tag{33}$$

$$\mathbf{B}_{\text{MEE}}(\mathbf{x}) = \begin{bmatrix} 0 & \frac{2p}{\sigma}\sqrt{\frac{p}{\mu}} & 0 & 0 \\ \sqrt{\frac{p}{\mu}}\,\sin l & \sqrt{\frac{p}{\mu}}\,\frac{1}{\sigma}\left[(\sigma+1)\,\cos l + e_x\right] & -\sqrt{\frac{p}{\mu}}\,\frac{e_y}{\sigma}\left(h_x\,\sin l - h_y\,\cos l\right) & 0 \\ -\sqrt{\frac{p}{\mu}}\,\cos l & \sqrt{\frac{p}{\mu}}\,\frac{1}{\sigma}\left[(\sigma+1)\,\sin l + e_y\right] & \sqrt{\frac{p}{\mu}}\,\frac{e_x}{\sigma}\left(h_x\,\sin l - h_y\,\cos l\right) & 0 \\ 0 & 0 & \sqrt{\frac{p}{\mu}}\,\frac{b^2}{2\,\sigma}\,\cos l & 0 \\ 0 & 0 & \sqrt{\frac{p}{\mu}}\,\frac{b^2}{2\,\sigma}\,\sin l & 0 \\ 0 & 0 & \sqrt{\frac{p}{\mu}}\,\frac{1}{\sigma}\,\left(h_x\,\sin l - h_y\,\cos l\right) & 0 \\ 0 & 0 & 0 & -\frac{1}{g_0\,I_{\text{sp}}} \end{bmatrix} \tag{34}$$

where

$$\sigma = 1 + e_x\,\cos l + e_y\,\sin l, \quad b^2 = 1 + h_y^2 + h_y^2 \tag{35}$$

Note that the control components are expressed in the standard local-vertical local-horizontal rotating frame the where the first axis is the radial unit vector $\mathbf{i}_r = \mathbf{r}/r$ that points along the position vector. The normal unit vector points in the orbit normal direction, and the transversal unit vector is found with the right-hand rule.

Modified Orbital Elements

We make use of another set of orbital elements that results in a linear representation in the unperturbed case. These modified orbital elements $[\Lambda, \eta, s, \gamma, \kappa, \Omega]$ can be derived from spherical

coordinates using[21]

$$\Lambda = \frac{p_h}{r} - \frac{\mu}{p_h}\sqrt{\frac{C}{\mu}} \tag{36}$$

$$\eta = p_r \sqrt{\frac{C}{\mu}} \tag{37}$$

$$s = \sin(\phi) \tag{38}$$

$$\gamma = \frac{p_\phi}{p_h}\cos(\phi) \tag{39}$$

$$\kappa = \frac{1}{p_h}\sqrt{\mu\, C} \tag{40}$$

where p_r, p_θ, and p_ϕ are the conjugate momenta of the corresponding Hamiltonian,

$$p_r = \dot{r} \tag{41}$$

$$p_\theta = r^2\,\dot{\theta}\,\cos^2(\phi) \tag{42}$$

$$p_\phi = r^2\,\dot{\phi} \tag{43}$$

and p_h is the angular momentum:

$$p_h = \sqrt{p_\phi^2 + \frac{p_\theta^2}{\cos^2(\phi)}} \tag{44}$$

r denotes the radial distance, θ and ϕ the azimuthal and polar angle, respectively. The standard gravitational parameter μ and some length unit C are included to make the quantities dimensionless. Ω is identical to the classical longitude of the ascending node. Note that a time regularization was performed that is defined as follows:

$$\mathrm{d}t = \frac{r^2}{p_h}\,\mathrm{d}\zeta \tag{45}$$

The time can thus be obtained by integrating the following differential equation:

$$\frac{\mathrm{d}t}{\mathrm{d}\zeta} = \frac{1}{\kappa(\kappa+\Lambda)^2}\sqrt{\frac{C^3}{\mu}} \tag{46}$$

As we are interested in fixed final time problems, the time t is included as an additional state. Therefore, the states are defined as

$$\mathbf{x} = [\Lambda, \eta, s, \gamma, \kappa, \Omega, w, t]^\top \tag{47}$$

Clearly, the unperturbed dynamics become nonlinear if the time is added as a state variable. With regard to the implementation, all quantities (including the perturbing accelerations, gravitational acceleration, and the specific impulse) are normalized before solving the optimization problem numerically. Therefore, the scaling factors C^2/μ and $\sqrt{C^3/\mu}$ are dropped in the remainder of this

work as they are already implicitly included. The quantities $\mathbf{g}_{\mathrm{MOE}}(\mathbf{x})$ and $\mathbf{B}_{\mathrm{MOE}}(\mathbf{x})$ in the ζ domain are then

$$\mathbf{g}_{\mathrm{MOE}}(\mathbf{x}) = \begin{bmatrix} -\eta \\ \Lambda \\ -s \\ \gamma \\ 0 \\ 0 \\ 0 \\ \frac{1}{\kappa\,(\kappa+\Lambda)^2} \end{bmatrix},\ \mathbf{B}_{\mathrm{MOE}}(\mathbf{x}) = \begin{bmatrix} 0 & \frac{2\kappa+\Lambda}{\kappa\,(\kappa+\Lambda)^3} & 0 & 0 \\ \frac{1}{\kappa\,(\kappa+\Lambda)^2} & 0 & 0 & 0 \\ 0 & 0 & \frac{\sqrt{1-s^2-\gamma^2}}{\kappa\,(\kappa+\Lambda)^3} & 0 \\ 0 & 0 & 0 & 0 \\ 0 & -\frac{1}{(\kappa+\Lambda)^3} & 0 & 0 \\ 0 & 0 & \frac{s}{(s^2+\gamma^2)\,\kappa\,(\kappa+\Lambda)^3} & 0 \\ 0 & 0 & 0 & -\frac{1}{g_0\,I_{\mathrm{sp}}}\ \frac{1}{\kappa(\kappa+\Lambda)^2} \\ 0 & 0 & 0 & 0 \end{bmatrix} \tag{48}$$

The control components are defined in the local-vertical local-horizontal rotating frame as in MEE.

Remark: As Ω is not defined for equatorial orbits, this coordinate set has a singularity when the inclination is close to zero. Yet, in the context of this paper, only problems where $i \neq 0$ are considered.

Kustaanheimo-Stiefel Coordinates

The Kustaanheimo-Stiefel transformation is based on Levi-Civita's regularization in three dimensions. The idea is to describe the equations of motion using complex numbers and quaternion algebra. The transformation between Cartesian $\mathbf{r} \in \mathbb{R}^3$ and non-minimal KS coordinates $\mathbf{p} = [p_1, p_2, p_3, p_4] \in \mathbb{R}^4$ is given by[20]

$$\mathbf{r} = \mathbf{L}(\mathbf{p})\,\mathbf{p} \tag{49}$$

$$\mathbf{r}' = 2\,\mathbf{L}(\mathbf{p})\,\mathbf{p}' \tag{50}$$

with

$$\mathbf{L}(\mathbf{p}) = \begin{bmatrix} p_1 & -p_2 & -p_3 & p_4 \\ p_2 & p_1 & -p_4 & -p_3 \\ p_3 & p_4 & p_1 & p_2 \\ p_4 & -p_3 & p_2 & -p_1 \end{bmatrix} \tag{51}$$

The inverse transformation can be obtained using the relation

$$[\mathbf{L}(\mathbf{p})]^{-1} = \frac{1}{r}\,[\mathbf{L}(\mathbf{p})]^{\top} \tag{52}$$

$(\cdot)' \coloneqq \frac{\mathrm{d}}{\mathrm{d}\xi}$ denotes a time regularization in the fictitious time domain ξ defined by

$$\mathrm{d}t = r\,\mathrm{d}\xi \tag{53}$$

where $r = \|\mathbf{r}\|_2 = \|\mathbf{p}\|_2^2$. This results in the following equation of a harmonic oscillator:

$$2\,\mathbf{p}'' + h\,\mathbf{p} = \|\mathbf{p}\|^2\,[\mathbf{L}(\mathbf{p})]^{\top} \begin{bmatrix} \boldsymbol{\tau} \\ 0 \end{bmatrix} \tag{54}$$

where h denotes the negative of the specific orbital energy:

$$h \coloneqq \frac{\mu}{r} - \frac{1}{2}\|\mathbf{v}\|^2 \tag{55}$$

The equations of motion then read:

$$\frac{\mathrm{d}\mathbf{p}}{\mathrm{d}\xi} = \mathbf{p}' \tag{56a}$$

$$\frac{\mathrm{d}\mathbf{p}'}{\mathrm{d}\xi} = -\frac{h}{2}\,\mathbf{p} + \frac{1}{2}\,\|\mathbf{p}\|_2^2\,[\mathbf{L}(\mathbf{p})]^\top \begin{bmatrix}\boldsymbol{\tau}\\ 0\end{bmatrix} \tag{56b}$$

$$\frac{\mathrm{d}h}{\mathrm{d}\xi} = -2\,[\mathbf{p}']^\top\,[\mathbf{L}(\mathbf{p})]^\top \begin{bmatrix}\boldsymbol{\tau}\\ 0\end{bmatrix} \tag{56c}$$

$$\frac{\mathrm{d}t}{\mathrm{d}\xi} = \|\mathbf{p}\|_2^2 \tag{56d}$$

The time regularization in Eq. (53) results in weakly nonlinear dynamics for the unperturbed case. Even though it is expected that this is already advantageous compared to coordinates that yield highly nonlinear equations of motion for the unperturbed case, it would be desirable to obtain linear dynamics when no perturbation is present. Therefore, we define another time regularization

$$\frac{\mathrm{d}}{\mathrm{d}t} = \frac{\sqrt{2h}}{r}\,\frac{\mathrm{d}}{\mathrm{d}E} \tag{57}$$

that results in linear unperturbed dynamics, E being the eccentric anomaly. As we want to compute fuel-optimal trajectories with fixed final time, the time t is included as an additional state. The state $\mathbf{x} \in \mathbb{R}^{11}$ and control $\mathbf{u} \in \mathbb{R}^4$ vectors then read

$$\mathbf{x}_{\mathrm{KS}}^{\xi} = \left[\mathbf{p}^\top, \mathbf{p}'^\top, h, w, t\right]^\top,\ \mathbf{x}_{\mathrm{KS}}^{E} = \left[\mathbf{p}^\top, \mathring{\mathbf{p}}^\top, h, w, t\right]^\top \tag{58}$$

$$\mathbf{u}_{\mathrm{KS}} = \left[\boldsymbol{\tau}^\top, \Gamma\right]^\top \tag{59}$$

where the superscripts ξ and E refer to the independent variables, and

$$\mathring{(\cdot)} \coloneqq \frac{\mathrm{d}}{\mathrm{d}E} \tag{60}$$

If ξ is the independent variable, the quantities $\mathbf{g}_{\mathrm{KS}}^{\xi}(\mathbf{x})$ and $\mathbf{B}_{\mathrm{KS}}^{\xi}(\mathbf{x})$ are

$$\mathbf{g}_{\mathrm{KS}}^{\xi}(\mathbf{x}) = \begin{bmatrix}\mathbf{p}'\\ -\frac{h}{2}\,\mathbf{p}\\ 0\\ 0\\ \|\mathbf{p}\|^2\end{bmatrix}, \quad \mathbf{B}_{\mathrm{KS}}^{\xi}(\mathbf{x}) = \begin{bmatrix} & & \mathbf{0}_{4\times 4} & \\ \frac{p_1}{2}\|\mathbf{p}\|^2 & \frac{p_2}{2}\|\mathbf{p}\|^2 & \frac{p_3}{2}\|\mathbf{p}\|^2 & 0\\ -\frac{p_2}{2}\|\mathbf{p}\|^2 & \frac{p_1}{2}\|\mathbf{p}\|^2 & \frac{p_4}{2}\|\mathbf{p}\|^2 & 0\\ -\frac{p_3}{2}\|\mathbf{p}\|^2 & -\frac{p_4}{2}\|\mathbf{p}\|^2 & \frac{p_1}{2}\|\mathbf{p}\|^2 & 0\\ \frac{p_4}{2}\|\mathbf{p}\|^2 & -\frac{p_3}{2}\|\mathbf{p}\|^2 & \frac{p_2}{2}\|\mathbf{p}\|^2 & 0\\ B_{\mathrm{KS},91}^{\xi} & B_{\mathrm{KS},92}^{\xi} & B_{\mathrm{KS},93}^{\xi} & 0\\ 0 & 0 & 0 & -\frac{\|\mathbf{p}\|^2}{g_0\,I_{\mathrm{sp}}}\\ 0 & 0 & 0 & 0\end{bmatrix} \tag{61}$$

where

$$B_{\mathrm{KS},91}^{\xi} = 2(-p_1p_1' + p_2p_2' + p_3p_3' - p_4p_4') \tag{62a}$$

$$B_{\mathrm{KS},92}^{\xi} = 2(-p_1p_2' - p_2p_1' + p_3p_4' + p_4p_3') \tag{62b}$$

$$B^{\xi}_{\mathrm{KS},93} = 2(-p_1 p'_3 - p_2 p'_4 - p_3 p'_1 - p_4 p'_2) \tag{62c}$$

If E is the independent variable, the quantities $\mathbf{g}^E_{\mathrm{KS}}(\mathbf{x})$ and $\mathbf{B}^E_{\mathrm{KS}}(\mathbf{x})$ are given by

$$\mathbf{g}^E_{\mathrm{KS}}(\mathbf{x}) = \begin{bmatrix} \mathring{\mathbf{p}} \\ -\frac{1}{4}\,\mathbf{p} \\ 0 \\ 0 \\ \frac{\|\mathbf{p}\|^2}{\sqrt{2h}} \end{bmatrix}, \quad \mathbf{B}^E_{\mathrm{KS}}(\mathbf{x}) = \begin{bmatrix} & & \mathbf{0}_{4\times 4} & \\ B^E_{\mathrm{KS},51} & B^E_{\mathrm{KS},52} & B^E_{\mathrm{KS},53} & 0 \\ B^E_{\mathrm{KS},61} & B^E_{\mathrm{KS},62} & B^E_{\mathrm{KS},63} & 0 \\ B^E_{\mathrm{KS},71} & B^E_{\mathrm{KS},72} & B^E_{\mathrm{KS},73} & 0 \\ B^E_{\mathrm{KS},81} & B^E_{\mathrm{KS},82} & B^E_{\mathrm{KS},83} & 0 \\ B^E_{\mathrm{KS},91} & B^E_{\mathrm{KS},92} & B^E_{\mathrm{KS},93} & 0 \\ 0 & 0 & 0 & -\frac{\|\mathbf{p}\|^2}{\sqrt{2h}\,g_0\,I_{\mathrm{sp}}} \\ 0 & 0 & 0 & 0 \end{bmatrix} \tag{63}$$

The expressions for the elements of $\mathbf{B}^E_{\mathrm{KS}}(\mathbf{x})$ are given in the appendix. Similar to MOE, the unperturbed dynamics become nonlinear if the time is added as a state variable.

In the planar case, the inverse KS transformation is unique, and the final boundary condition is simply a linear equality constraint. In the spatial case, however, there is an additional degree of freedom. Therefore, one element of $\mathbf{p}$ can be chosen arbitrarily. This means that the fixed final state $\mathbf{p}_f$ depends on the initial condition $\mathbf{p}_0$, and its value is to be obtained by integrating the dynamics. As a consequence, the final boundary condition is not a linear equality constraint anymore, but a nonlinear function of the initial condition. In discretized form, the final state $[\mathbf{p}(t_f)]^\top, [\mathbf{p}'(t_f)]^\top$ can be mapped from KS to Cartesian coordinates, and the target state can be imposed in Cartesian coordinates:

$$\begin{bmatrix} \mathbf{r}_f \\ \mathbf{v}_f \end{bmatrix} = \mathcal{M}^{\xi}[\mathbf{p}(t_f), \mathbf{p}'(t_f)] \tag{64}$$

where $\mathcal{M}^{\xi}$ denotes the nonlinear mapping from KS to Cartesian coordinates according to Eqs. (49), (50) and (52), respectively. The new final boundary conditions then read

$$\mathbf{r}_f = \mathbf{L}[\mathbf{p}(t_f)]\,\mathbf{p}(t_f), \quad \mathbf{v}_f = \frac{2}{\|\mathbf{p}(t_f)\|^2}\,\mathbf{L}[\mathbf{p}(t_f)]\,\mathbf{p}'(t_f) \tag{65}$$

They are linearized about the reference and added in the optimization. The final boundary conditions for the independent variable E are defined accordingly. The controls are expressed in the Cartesian coordinate frame.

NUMERICAL SIMULATIONS

The impact of the coordinate sets is assessed in two analyses:

1. Nonlinearity index: the two indices Ξ^f and Ξ^x are determined and compared for all coordinate sets.

2. Reliability: using initial guesses of different quality, we compute hundreds of optimal trajectories using each set to compare the success rate, number of iterations, final mass, and CPU time.

Table 2: Simulation values for the transfers to the asteroids 2000 SG344[22] and Dionysus.[23]

Parameter	SEL_2 to 2000 SG344	Earth to Dionysus
Initial epoch	04-Feb-2024 12:00:00 UTC	23-Dec-2012 00:00:00 UTC
Initial position $\mathbf{r}_0$, AU	$[-0.701\,860\,65,\ 0.647\,969\,56,\ 0.280\,890\,92]^\top$	$[-0.023\,729\,65,\ 0.902\,196\,12,\ 0.391\,115\,96]^\top$
Initial velocity $\mathbf{v}_0$, VU	$[-0.732\,969\,49,\ -0.656\,847\,37,\ -0.284\,730\,20]^\top$	$[-1.015\,931\,25,\ -0.025\,848\,08,\ -0.011\,168\,60]^\top$
Initial mass m_0, kg	22.6	4000
Final position $\mathbf{r}_f$, AU	$[0.418\,067\,95,\ 0.761\,136\,49,\ 0.328\,430\,28]^\top$	$[-2.040\,620\,09,\ 1.661\,992\,01,\ 1.324\,703\,65]^\top$
Final velocity $\mathbf{v}_f$, VU	$[-0.969\,903\,32,\ 0.400\,790\,22,\ 0.172\,419\,04]^\top$	$[-0.142\,318\,14,\ -0.421\,402\,69,\ -0.162\,049\,85]^\top$
Final mass $m(t_f)$, kg	free	free
Max. thrust $T_{\max}$, N	2.2519×10^{-3}	0.32
Sp. impulse I_{sp}, s	3067	3000
Time of flight t_f, days	700	3534

We consider fuel-optimal transfers from the Sun-Earth Lagrange Point L_2 (SEL_2) to asteroid 2000 SG344, and from Earth to asteroid Dionysus. The J2000 reference frame is used where the xy-plane lies in the equatorial plane. The maximum thrust $T_{\max}$ and specific impulse I_{sp} are assumed constant. Relevant parameters are given in Table 2. All simulations are performed in MATLAB version 2018b on an Intel Core i5-6300 2.30 GHz Laptop with four cores and 8 GB of RAM.

Using the procedure explained in Section III, $N = 500$ perturbed state and control trajectories are generated. The following variations are considered in this work:

$$\begin{aligned} \text{2000 SG344:}\quad & \delta\mathbf{r}_{\max} = \left[10^5, 10^5, 10^5\right]^\top \text{km},\ \delta\mathbf{v}_{\max} = \left[10^{-2}, 10^{-2}, 10^{-2}\right]^\top \text{km}\,\text{s}^{-1}, \\ & \delta\boldsymbol{\tau}_{\max} = [1.2, 1.2, 1.2]^\top \times 10^{-6}\,\text{km}\,\text{s}^{-2} \end{aligned} \tag{66}$$

$$\begin{aligned} \text{Dionysus:}\quad & \delta\mathbf{r}_{\max} = \left[10^6, 10^6, 10^6\right]^\top \text{km},\ \delta\mathbf{v}_{\max} = \left[10^{-1}, 10^{-1}, 10^{-1}\right]^\top \text{km}\,\text{s}^{-1}, \\ & \delta\boldsymbol{\tau}_{\max} = [8.9, 8.9, 8.9]^\top \times 10^{-8}\,\text{km}\,\text{s}^{-2} \end{aligned} \tag{67}$$

Typical reference and perturbed trajectories are shown in Figs. 3 and 4. The obtained trajectories are used to determine the nonlinearity indices and serve as the initial guesses for the reliability analysis. Throughout this section, we use Cart, Sph, Cyl, MEE, MOE, KS_ξ, and KS_E to refer to the coordinate sets described in Section IV.

Remark: For the 2000 SG344 transfer, the control variations are several times larger than the maximum control magnitude of the reference trajectory. The reason is that smaller values would result in success rates of $100\,\%$ for all sets, which is not desirable for assessing the reliability.

Nonlinearity Index

The nonlinearity indices Ξ^f and Ξ^x are computed according to Eqs. (5) and (11). Their evolution for the transfers to asteroids 2000 SG344 and Dionysus are shown in Figs. 5 and 6, respectively. The values of Ξ^f and Ξ^x take different orders of magnitude over time, and Cartesian coordinates

Table 3: Parameters of the SCP algorithm.

Parameter	Value
Feasibility tol. ε_c	10^{-6}
Optimality tol. ε_ϕ	10^{-4}
Max. iterations	150
λ	10.0
ρ_0, ρ_1, ρ_2	0.01, 0.25, 0.85
α, β	1.5, 1.5

Table 4: Physical constants in all simulations.

Parameter	Value
Gravitational const. μ	$1.327\,124\,4 \times 10^{11}\,\mathrm{km^3\,s^{-2}}$
Gravitational accel. g_0	$9.806\,65 \times 10^{-3}\,\mathrm{km\,s^{-2}}$
Length unit AU	$1.495\,978\,707 \times 10^{8}\,\mathrm{km}$
Velocity unit VU	$\sqrt{\mu/\mathrm{AU}}$
Time unit TU	AU/VU
Acceleration unit ACU	VU/TU
Mass unit MU	m_0

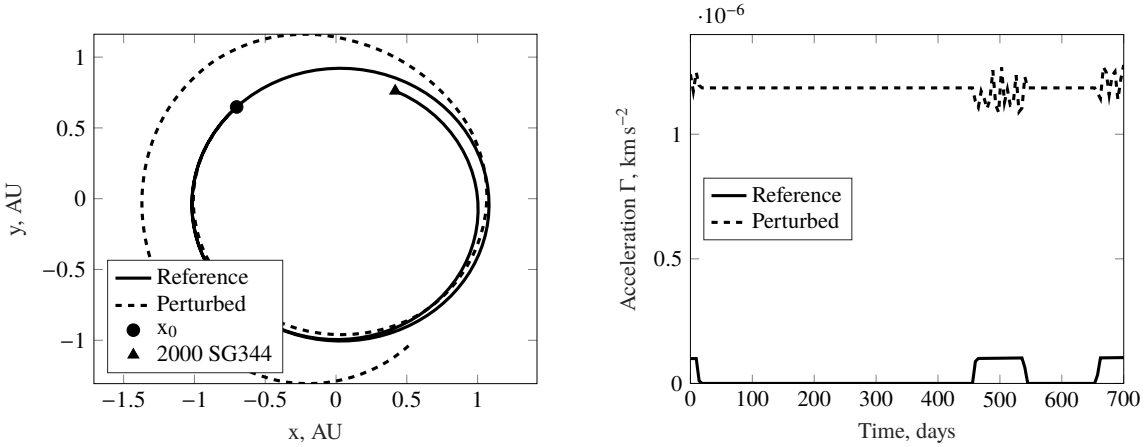

(a) Transfer trajectory.

(b) Control acceleration.

Figure 3: Typical reference and perturbed state and control trajectories for 2000 SG344.

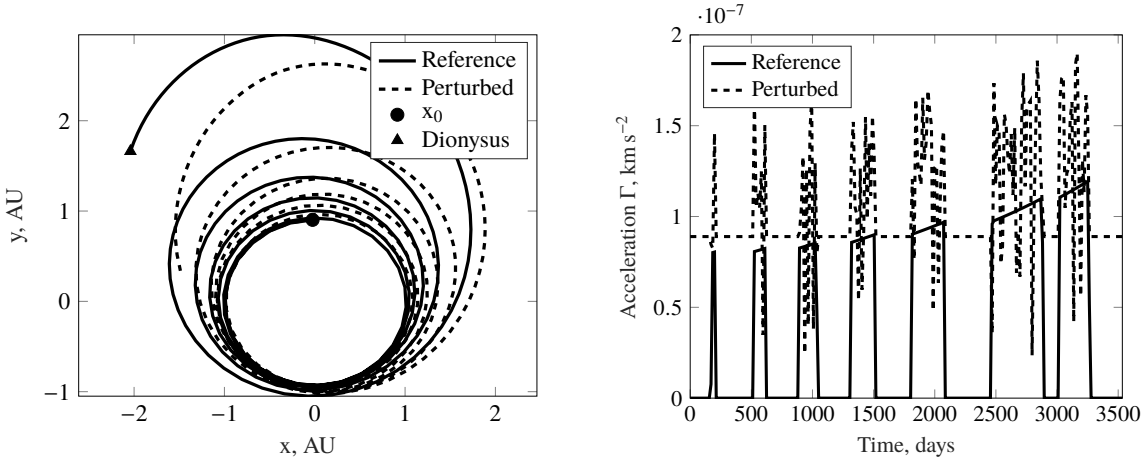

(a) Transfer trajectory.

(b) Control acceleration.

Figure 4: Typical reference and perturbed state and control trajectories for Dionysus.

result in considerably larger values than the other coordinate sets. These, instead, yield relatively similar values (especially in the case of asteroid 2000 SG344). With regard to Ξ^x, the discrepancy between Cartesian and the other coordinates is even more significant. As the acceleration due to thrust is small with respect to the unperturbed two-body dynamics, it is reasonable that coordinate sets with highly nonlinear unperturbed dynamics (such as Cartesian) reach larger values. In general, it appears that MOE and cylindrical elements result in the smallest indices, directly followed by spherical and MEE. Surprisingly, KS_ξ and KS_E take rather large values despite their (quasi-)linear dynamics. This may be due to the complex and highly nonlinear expressions for the $\mathbf{B}(\mathbf{x})$ matrices in combination with the larger number of states, including time.

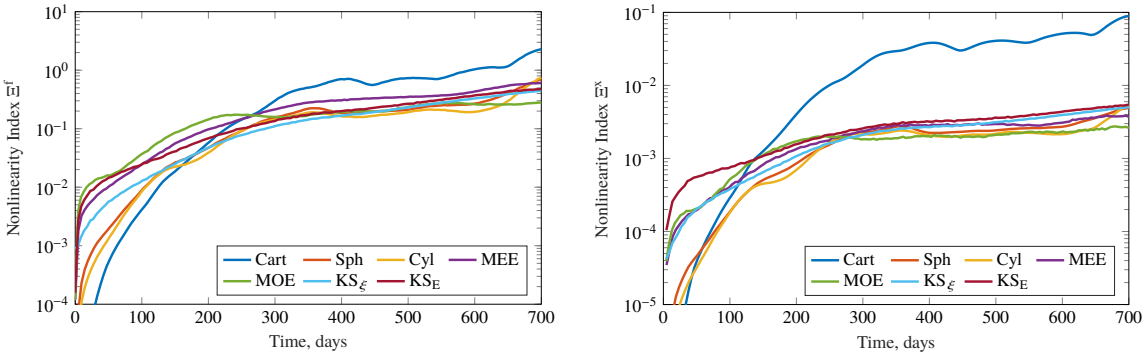

(a) Nonlinearity index Ξ^f.

(b) Nonlinearity index Ξ^x.

Figure 5: Nonlinearity indices for 2000 SG344.

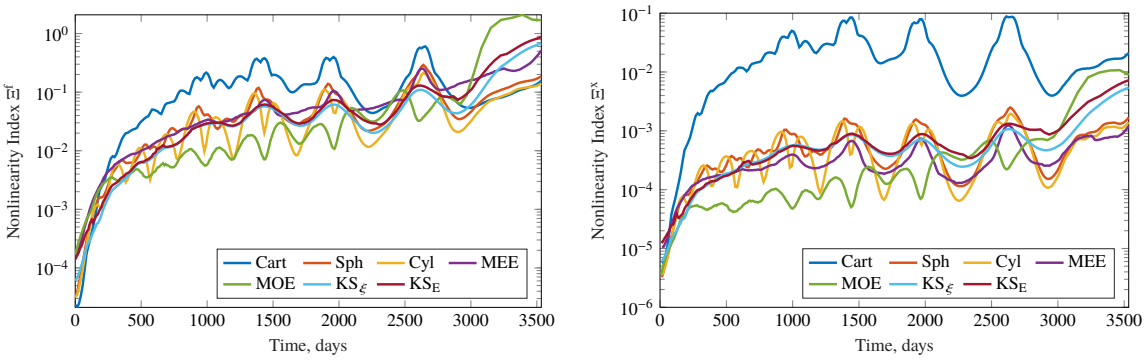

(a) Nonlinearity index Ξ^f.

(b) Nonlinearity index Ξ^x.

Figure 6: Nonlinearity indices for Dionysus.

Reliability Analysis

The convexified optimization problem is solved using the open-source Embedded Conic Solver (ECOS).[24] Parameters of the SCP algorithm are given in Table 3, physical constants for the normalization in Table 4. The algorithm converges if the maximum constraint violation and the change of the objective function are smaller than the thresholds ε_c and ε_ϕ, respectively. ρ_i $(i = 0, 1, 2)$ and α, β are trust-region parameters.[25,26]

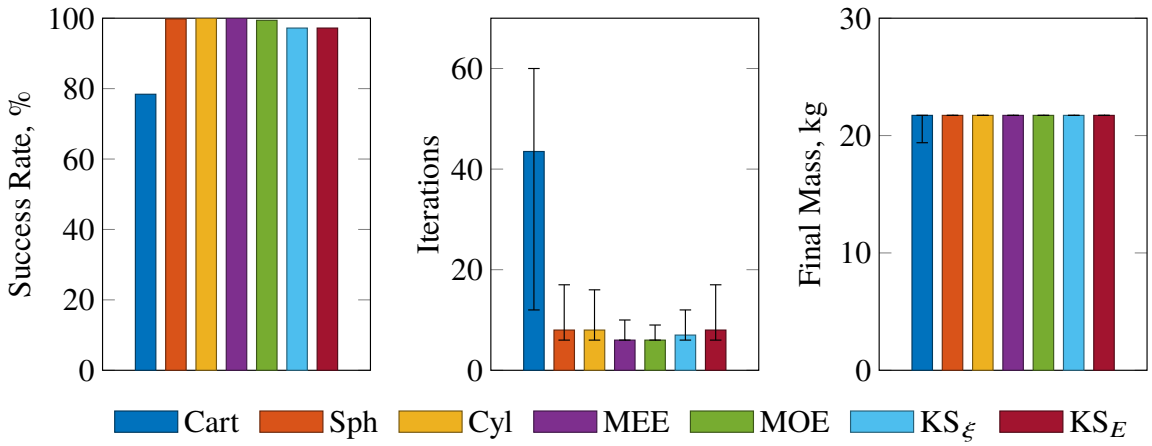

Figure 7: Comparison of success rate, iterations, and final mass for 2000 SG344 (fixed final value of the independent variable for MOE and KS).

With regard to the transfer to asteroid 2000 SG344, the comparison of the success rate, number of iterations, and final mass for the 500 simulations is shown in Fig. 7. Median values are presented, and the error bars refer to the $90\,\%$ percentile of the respective quantity. Note that we assume the final value of the independent variable for MOE and KS to be fixed and known, e.g. from a previous optimization. All methods despite Cartesian coordinates (success rate of only $80\,\%$) converge in almost all cases, KS yielding slightly fewer optimal solutions compared to Sph, Cyl, MEE, and MOE. Cartesian elements require significantly more iterations than all other sets. The final mass is instead similar.

For Dionysus, Sph, Cyl, MEE, and MOE outperform the other state representations in terms of success rate. Remarkably, all simulations converged successfully for MOE. Interestingly, Cart, Sph, Cyl, MEE, and KS$_\xi$ require a similar amount of iterations (around 30), whereas MOE and KS$_E$ need only approximately five iterations. All methods yield a similar final mass.

The success rates seem to be in accordance with the nonlinearity index, because the highest success rates are obtained with MOE, Cyl, Sph, and MEE, which also yield the smallest indices. Even though both KS sets result in similar indices compared to Sph, Cyl, and MEE, the additional nonlinear final boundary constraint is probably the reason for the fewer converged cases. Moreover, MOE and KS$_E$ represent the only coordinate sets with linear unperturbed dynamics (except for the differential equation of the time) according to Table 1. Since the SCP process is based on linearization, it is reasonable that they are able to solve the considered problems in fewer iterations. This is particularly true for MOE, which has fewer state variables than KS$_E$ and linear final boundary conditions, thus resulting in a higher success rate. As the independent variables of MOE and KS are anomaly-like quantities, their final values may not be known in advance. Instead of keeping the final value of the independent variable fixed, the problem can be transformed into a free independent variable problem (keeping in mind that the independent variable is not time, and that the actual time of flight does not change). This way, the final value of the independent variable is free, and therefore, an additional degree of freedom is added that might be beneficial for the solver. Figure 9 shows the results for the Dionysus transfer. It is evident that the success rates increase from $80\,\%$ to $98\,\%$ (KS$_\xi$) and from $79\,\%$ to $91\,\%$ (KS$_E$). As a consequence, the variations in the number of iterations and final mass rise considerably as different solutions are found that are not close to the

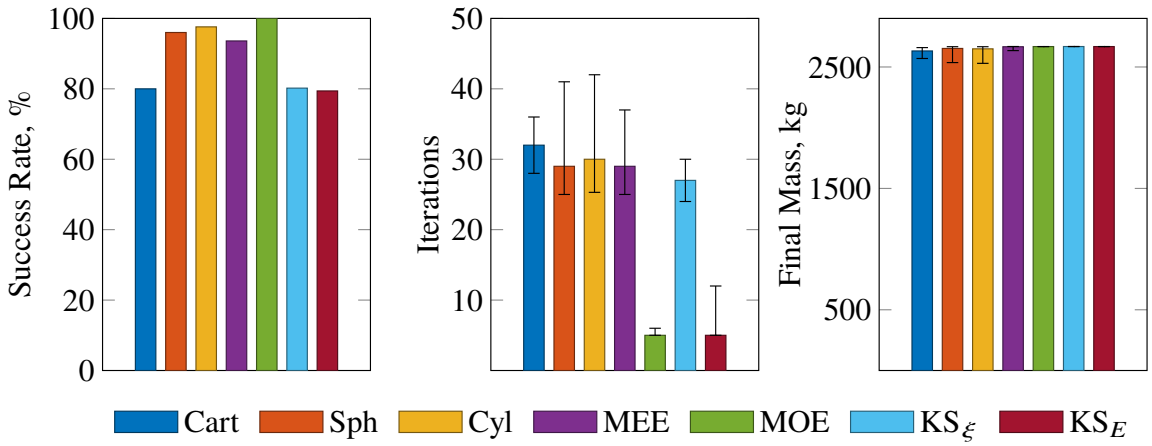

Figure 8: Comparison of success rate, iterations, and final mass for Dionysus (fixed final value of the independent variable for MOE and KS).

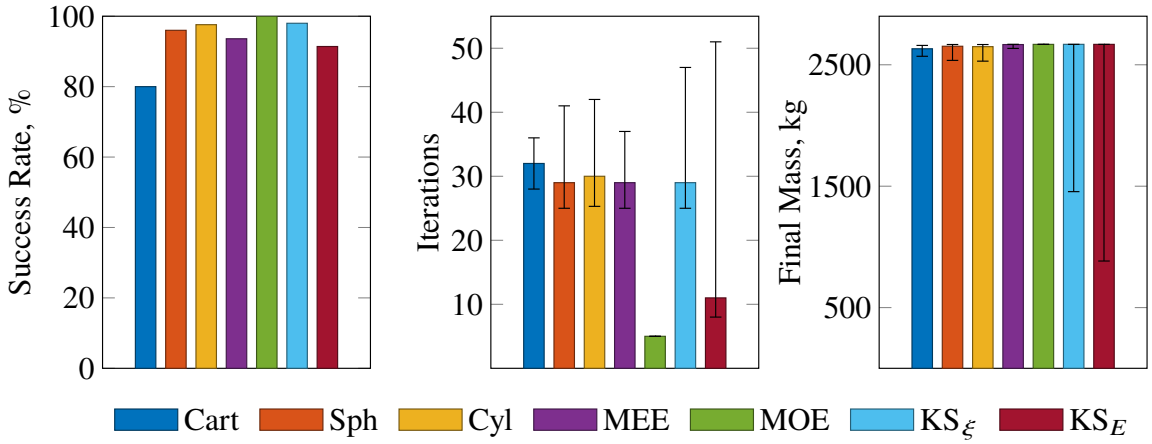

Figure 9: Comparison of success rate, iterations, and final mass for Dionysus (free final value of the independent variable for MOE and KS).

reference. Still, keeping the final value of the independent variable free can be an effective means to increase convergence for KS. The results for the 2000 SG344 transfer do not change significantly compared to the fixed independent variable case.

As expected, the median CPU time per simulation in Fig. 10a follows the same trend as the number of iterations. Yet, the CPU time per SCP iteration in Fig. 10b differs: KS$_\xi$ and KS$_E$ require more time per iteration due to the larger number of states, and hence larger matrices. KS$_E$ is the worst state representation in terms of CPU time per iteration due to the more complex control matrix $\mathbf{B}(\mathbf{x})$ compared to KS$_\xi$. Remarkably, MOE requires a similar amount of time compared to standard sets despite the additional state.

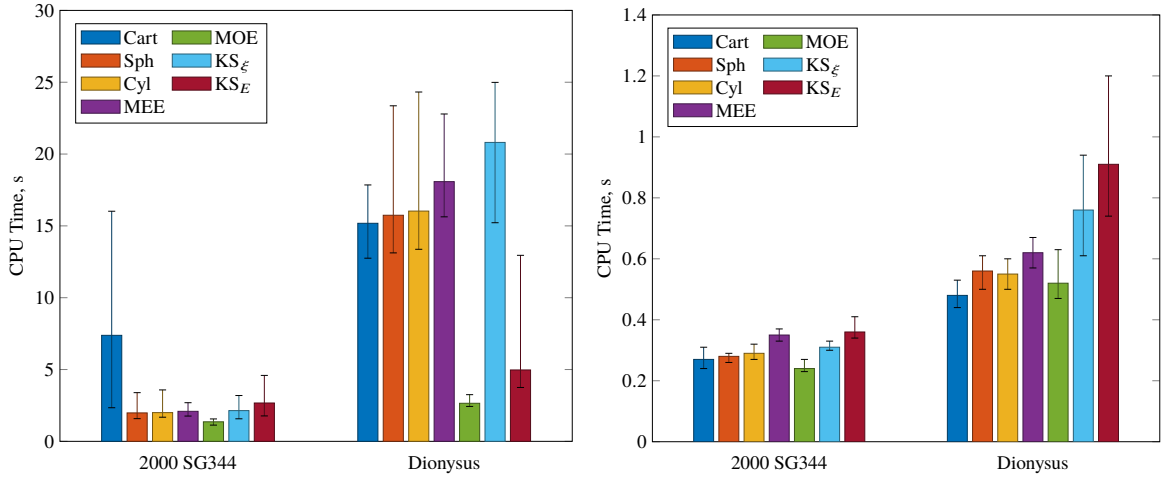

(a) Total CPU time.

(b) CPU time per major SCP iteration.

Figure 10: Comparison of Total CPU time and CPU time per iteration.

CONCLUSION

In this work, several coordinate sets are assessed for the convex low-thrust trajectory optimization problem. The most popular standard coordinates, and three non-standard state vector representations that result in (quasi-)linear unperturbed dynamics are considered. This thorough comparison can serve as a reference for other researchers as convex programming techniques are becoming more and more important in the aerospace community. Our simulations suggest that MOE, MEE, spherical, and cylindrical coordinates outperform Cartesian coordinates in terms of success rate. Sets with an independent variable different from time that have linear unperturbed dynamics such as MOE and KS_E require significantly fewer iterations. Moreover, the findings obtained in our extensive simulations are consistent with the indications provided by the proposed nonlinearity indices. These can be an effective indicator of the nonlinearity of a set of differential equations, and therefore of the performance of SCP when considering different state vector representations.

ACKNOWLEDGMENTS

This research is part of EXTREMA, a project that has received funding from the European Research Council (ERC) under the European Union's Horizon 2020 research and innovation programme (Grant Agreement No. 864697).

APPENDIX: ADDITIONAL EQUATIONS FOR COORDINATES

The entries of the $\mathbf{B}^E_{\mathrm{KS}}(\mathbf{x})$ matrix in Eq. (63) are as follows:

$$B^E_{\mathrm{KS},51} = \frac{1}{4h}\left(-4p_2\mathring{p}_1\mathring{p}_2 - 4p_3\mathring{p}_1\mathring{p}_3 + 4p_4\mathring{p}_1\mathring{p}_4 + 4p_1\mathring{p}_1^2 + p_1\|\mathbf{p}\|^2\right) \tag{68a}$$

$$B^E_{\mathrm{KS},52} = \frac{1}{4h}\left(4p_2\mathring{p}_1^2 + 4p_1\mathring{p}_1\mathring{p}_2 - 4p_4\mathring{p}_1\mathring{p}_3 - 4p_3\mathring{p}_1\mathring{p}_4 + p_2\|\mathbf{p}\|^2\right) \tag{68b}$$

$$B^E_{\mathrm{KS},53} = \frac{1}{4h}\left(4p_3\mathring{p}_1^2 + 4p_1\mathring{p}_1\mathring{p}_3 + 4p_4\mathring{p}_1\mathring{p}_2 + 4p_2\mathring{p}_1\mathring{p}_4 + p_3\|\mathbf{p}\|^2\right) \tag{68c}$$

$$B^E_{\mathrm{KS},61} = \frac{1}{4h}\left(4p_1\mathring{p}_1\mathring{p}_2 - 4p_3\mathring{p}_2\mathring{p}_3 + 4p_4\mathring{p}_2\mathring{p}_4 - 4p_2\mathring{p}_2^2 - p_2\|\mathbf{p}\|^2\right) \tag{68d}$$

$$B^E_{\mathrm{KS},62} = \frac{1}{4h}\left(4p_2\mathring{p}_1\mathring{p}_2 - 4p_4\mathring{p}_2\mathring{p}_3 - 4p_3\mathring{p}_2\mathring{p}_4 + 4p_1\mathring{p}_2^2 + p_1\|\mathbf{p}\|^2\right) \tag{68e}$$

$$B^E_{\mathrm{KS},63} = \frac{1}{4h}\left(4p_3\mathring{p}_1\mathring{p}_2 + 4p_1\mathring{p}_2\mathring{p}_3 + 4p_4\mathring{p}_2^2 + 4p_2\mathring{p}_2\mathring{p}_4 + p_4\|\mathbf{p}\|^2\right) \tag{68f}$$

$$B^E_{\mathrm{KS},71} = \frac{1}{4h}\left(4p_1\mathring{p}_1\mathring{p}_3 - 4p_2\mathring{p}_2\mathring{p}_3 - 4p_3\mathring{p}_3^2 + 4p_4\mathring{p}_3\mathring{p}_4 - p_3\|\mathbf{p}\|^2\right) \tag{68g}$$

$$B^E_{\mathrm{KS},72} = \frac{1}{4h}\left(4p_2\mathring{p}_1\mathring{p}_3 + 4p_1\mathring{p}_2\mathring{p}_3 - 4p_4\mathring{p}_3^2 - 4p_3\mathring{p}_3\mathring{p}_4 - p_4\|\mathbf{p}\|^2\right) \tag{68h}$$

$$B^E_{\mathrm{KS},73} = \frac{1}{4h}\left(4p_3\mathring{p}_1\mathring{p}_3 + 4p_1\mathring{p}_3^2 + 4p_4\mathring{p}_2\mathring{p}_3 + 4p_2\mathring{p}_3\mathring{p}_4 + p_1\|\mathbf{p}\|^2\right) \tag{68i}$$

$$B^E_{\mathrm{KS},81} = \frac{1}{4h}\left(4p_1\mathring{p}_1\mathring{p}_4 - 4p_2\mathring{p}_2\mathring{p}_4 - 4p_3\mathring{p}_3\mathring{p}_4 + 4p_4\mathring{p}_4^2 + p_4\|\mathbf{p}\|^2\right) \tag{68j}$$

$$B^E_{\mathrm{KS},82} = \frac{1}{4h}\left(4p_2\mathring{p}_1\mathring{p}_4 + 4p_1\mathring{p}_2\mathring{p}_4 - 4p_4\mathring{p}_3\mathring{p}_4 - 4p_3\mathring{p}_4^2 - p_3\|\mathbf{p}\|^2\right) \tag{68k}$$

$$B^E_{\mathrm{KS},83} = \frac{1}{4h}\left(4p_3\mathring{p}_1\mathring{p}_4 + 4p_1\mathring{p}_3\mathring{p}_4 + 4p_4\mathring{p}_2\mathring{p}_4 + 4p_2\mathring{p}_4^2 + p_2\|\mathbf{p}\|^2\right) \tag{68l}$$

$$B^E_{\mathrm{KS},91} = -2\left(p_1\mathring{p}_1 - p_2\mathring{p}_2 - p_3\mathring{p}_3 + p_4\mathring{p}_4\right) \tag{68m}$$

$$B^E_{\mathrm{KS},92} = -2\left(p_2\mathring{p}_1 + p_1\mathring{p}_2 - p_4\mathring{p}_3 - p_3\mathring{p}_4\right) \tag{68n}$$

$$B^E_{\mathrm{KS},93} = -2\left(p_3\mathring{p}_1 + p_1\mathring{p}_3 + p_4\mathring{p}_2 + p_2\mathring{p}_4\right) \tag{68o}$$

REFERENCES

[1] J. L. Junkins and E. Taheri, "Exploration of Alternative State Vector Choices for Low-Thrust Trajectory Optimization," *Journal of Guidance, Control, and Dynamics*, Vol. 42, No. 1, 2019, pp. 47–64, 10.2514/1.G003686.

[2] F. Topputo and C. Zhang, "Survey of Direct Transcription for Low-Thrust Space Trajectory Optimization with Applications," *Abstract and Applied Analysis*, Vol. 2014, 2014, pp. 1–15, 10.1155/2014/851720.

[3] Z. Wang and M. J. Grant, "Optimization of Minimum-Time Low-Thrust Transfers Using Convex Programming," *Journal of Spacecraft and Rockets*, Vol. 55, No. 3, 2018, pp. 586–598, 10.2514/1.A33995.

[4] Z. Wang and M. J. Grant, "Minimum-Fuel Low-Thrust Transfers for Spacecraft: A Convex Approach," *IEEE Transactions on Aerospace and Electronic Systems*, Vol. 54, No. 5, 2018, pp. 2274–2290, 10.1109/TAES.2018.2812558.

[5] E. Taheri and O. Abdelkhalik, "Initial Three-Dimensional Low-Thrust Trajectory Design," *Advances in Space Research*, Vol. 57, No. 3, 2016, pp. 889 – 903, 10.1016/j.asr.2015.11.034.

[6] M. Lara, J. F. San-Juan, and L. M. López-Ochoa, "Delaunay Variables Approach to the Elimination of the Perigee in Artificial Satellite Theory," *Celestial Mechanics and Dynamical Astronomy*, Vol. 120, No. 1, 2014, pp. 39–56, 10.1007/s10569-014-9559-2.

[7] D. A. Vallado, *Fundamentals of Astrodynamics and Applications*. Microcosm Press, 4 ed., 2013.

[8] R. A. Broucke and P. J. Cefola, "On the equinoctial orbit elements," *Celestial Mechanics*, Vol. 5, No. 3, 1972, pp. 303–310, 10.1007/BF01228432.

[9] J. T. Betts, "Optimal Low–Thrust Orbit Transfers With Eclipsing," *Optimal Control Applications and Methods*, Vol. 36, No. 2, 2015, pp. 218–240, 10.1002/oca.2111.

[10] E. Taheri, I. Kolmanovsky, and E. Atkins, "Enhanced Smoothing Technique for Indirect Optimization of Minimum-Fuel Low-Thrust Trajectories," *Journal of Guidance, Control, and Dynamics*, Vol. 39, No. 11, 2016, pp. 2500–2511, 10.2514/1.g000379.

[11] B. Pan, P. Lu, X. Pan, and Y. Ma, "Double-Homotopy Method for Solving Optimal Control Problems," *Journal of Guidance, Control, and Dynamics*, Vol. 39, 6 2016, pp. 1706–1720, 10.2514/1.G001553.

[12] J. Roa and N. J. Kasdin, "Alternative Set of Nonsingular Quaternionic Orbital Elements," *Journal of Guidance, Control, and Dynamics*, Vol. 40, No. 11, 2017, pp. 2737–2751, 10.2514/1.G002753.

[13] S. Sreesawet and A. Dutta, "Fast and Robust Computation of Low-Thrust Orbit-Raising Trajectories," *Journal of Guidance, Control, and Dynamics*, Vol. 41, No. 9, 2018, pp. 1888–1905, 10.2514/1.G003319.

[14] J. L. Junkins and P. Singla, "How Nonlinear is it? A Tutorial on Nonlinearity of Orbit and Attitude Dynamics," *The Journal of the Astronautical Sciences*, Vol. 52, No. 1, 2004, pp. 7–60, 10.1007/BF03546420.

[15] A. Omran and B. Newman, "Nonlinearity Index Theory for Aircraft Dynamic Assessment," *Journal of Guidance, Control, and Dynamics*, Vol. 36, No. 1, 2013, pp. 293–303, 10.2514/1.53906.

[16] P. Kelly, V. Arya, J. L. Junkins, and M. Manoranjan, "Nonlinearity Index for State-Costate Dynamics of Optimal Control Problems," *2022 AAS/AIAA Astrodynamics Specialist Conference*, Charlotte, NC, USA, 2022. Paper AAS-22-830.

[17] C. Hofmann, A. C. Morelli, and F. Topputo, "Performance Assessment of Convex Low-Thrust Trajectory Optimization Methods," *Journal of Spacecraft and Rockets*, 2022. Advanced online publication, 10.2514/1.A35461.

[18] C. Hofmann and F. Topputo, "Rapid Low-Thrust Trajectory Optimization in Deep Space Based On Convex Programming," *Journal of Guidance, Control, and Dynamics*, Vol. 44, No. 7, 2021, pp. 1379–1388, 10.2514/1.G005839.

[19] D. Arnas and R. Linares, "Approximate Analytical Solution to the Zonal Harmonics Problem Using Koopman Operator Theory," *Journal of Guidance, Control, and Dynamics*, Vol. 44, No. 11, 2021, pp. 1909–1923, 10.2514/1.G005864.

[20] E. L. Stiefel and G. Scheifele, *Linear And Regular Celestial Mechanics*. 1971.

[21] D. Arnas and R. Linares, "Approximate Analytical Solution to the Zonal Harmonics Problem Using Koopman Operator Theory," *Journal of Guidance, Control, and Dynamics*, Vol. 44, No. 11, 2021, pp. 1909–1923, 10.2514/1.G005864.

[22] F. Topputo, Y. Wang, G. Giordano, V. Franzese, H. Goldberg, F. Perez-Lissi, and R. Walker, "Envelop of Reachable Asteroids by M-ARGO CubeSat," *Advances in Space Research*, Vol. 67, No. 12, 2021, pp. 4193–4221, 10.1016/j.asr.2021.02.031.

[23] E. Taheri, I. Kolmanovsky, and E. Atkins, "Enhanced Smoothing Technique for Indirect Optimization of Minimum-Fuel Low-Thrust Trajectories," *Journal of Guidance, Control, and Dynamics*, Vol. 39, No. 11, 2016, 10.2514/1.G000379.

[24] A. Domahidi, E. Chu, and S. Boyd, "ECOS: An SOCP Solver for Embedded Systems," *European Control Conference*, Zurich, Switzerland, 2013, pp. 3071–3076, doi: 10.23919/ECC.2013.6669541.

[25] C. Hofmann and F. Topputo, "Toward On-Board Guidance of Low-Thrust Spacecraft in Deep Space Using Sequential Convex Programming," *Proceedings of AAS/AIAA Space Flight Mechanics Meeting AAS Paper 21-350*, Feb. 2021, pp. 1–19.

[26] Y. Mao, M. Szmuk, X. Xu, and B. Açıkmeşe, "Successive Convexification: A Superlinearly Convergent Algorithm for Non-convex Optimal Control Problems," `https://arxiv.org/abs/1804.06539`, Preprint, submitted February 2019.